PSFC/JA-14-48

High Density LHRF Experiments in Alcator C-Mod and Implications for Reactor Scale Devices

S. G. Baek, R. R. Parker, P. T. Bonoli, S. Shiraiwa,
G. M. Wallace, B. LaBombard, I. C. Faust,
M. Porkolab, D. G. Whyte

December, 2014

Plasma Science and Fusion Center
Massachusetts Institute of Technology
Cambridge MA 02139 USA

This work was supported by the U.S. Department of Energy, Grant No. DEFC02-99ER54512.

High Density LHRF Experiments in Alcator C-Mod and Implications for Reactor Scale Devices

S. G. Baek, R. R. Parker, P. T. Bonoli, S. Shiraiwa, G. M. Wallace, B. LaBombard, I. C. Faust, M. Porkolab, D. G. Whyte

Plasma Science and Fusion Center, MIT, Cambridge, MA 02139 USA

E-mail: sgbaek@psfc.mit.edu

Abstract. Parametric Decay Instabilities (PDI) appear to be an ubiquitous feature of Lower Hybrid Current Drive (LHCD) experiments at high density. In density ramp experiments in Alcator C-Mod and other machines the onset of PDI activity has been well correlated with a decrease in current drive efficiency and production of fast electron Bremsstrahlung. However whether PDI is the primary cause of the "density limit", and if so by exactly what mechanism (beyond the obvious one of pump depletion) has not been clearly established. In order to further understand the connection, the frequency spectrum of PDI activity occurring during Alcator C-Mod LHCD experiments has been explored in detail by means of a number of RF probes distributed around the periphery of the C-Mod tokamak including a probe imbedded in the inner wall. The results show that i) the excited spectra consists mainly of a few discrete ion cyclotron quasi-modes, which have higher growth than the ion sound branch; ii) PDI activity can begin either at the inner or outer wall, depending on magnetic configuration; iii) the frequencies of the IC quasi-modes correspond to the magnetic field strength close to the LFS or HFS separatrix; and iv) although PDI activity may initiate near the inner separatrix, the loss in fast electron Bremsstrahlung is best correlated with the appearance of IC quasi-modes characteristic of the magnetic field strength near the LFS separatrix. These data, supported by growth rate calculations, point to the importance of the LFS SOL density in determining PDI onset and degradation in current drive efficiency. By minimizing the SOL density it is possible to extend the core density regime over which PDI can be avoided, thus potentially maximizing the effectiveness of LHCD at high density. Increased current drive efficiency at high density has been achieved in FTU and EAST through lithium coating and special fueling methods, and in recent C-Mod experiments by operating at higher plasma current. Another approach would be to locate the launcher in the inner wall with double null operation. This would reduce the SOL density by an order of magnitude or more and greatly mitigate the effects of PDI as well as other parasitic losses.

1. Introduction

Since the earliest days of Lower Hybrid Current Drive (LHCD) experiments, Parametric Decay Instabilities (PDI) have been linked to the sudden loss of suprathermal electrons and current drive efficiency as the density is increased above a critical density, n_{crit} [1-5]. In previous work [4-6] PDI effects have been observed to be important in the limit $\omega_0/\omega_{LH}(0) < 2$, where ω_0 is the applied LH frequency and $\omega_{LH}(0)$ is the lower hybrid frequency ($= \omega_{pi}/\sqrt{1 + \omega_{pe}^2/\omega_{ce}^2}$) evaluated on axis. However, an anomalous loss of current drive efficiency has nevertheless been observed in a number of tokamaks even though $\omega_0/\omega_{LH}(0) > 2$ and the accessibility condition [7] was well satisfied [8,9]. For example, an efficient current drive regime [10-12] on Alcator C-Mod ($R_0 \approx 67$ cm, $a \approx 22$ cm) [13] is found to exist only below the line-averaged density ($\bar{n}_e$) of $n_{crit} \approx 1 \times 10^{20}\ m^{-3}$ [14-16], for which $\omega_0/\omega_{LH}(0) = 3$ and the accessibility condition assures core LH penetration up to $\bar{n}_e \approx 1.5 \times 10^{20}\ m^{-3}$ for the typical launched parallel refractive index, $n_{||} = 2$, and B_T =5.4 T. Here, $n_{||} = ck_{||}/\omega_0$ is the ratio of the speed of light to the parallel phase velocity of the wave. Two simulations [16,17] showed that the inclusion of collisional damping and/or full-wave effects could partially explain the rapid loss of current drive efficiency, but these mechanisms alone still over-predict the level of the fast electron Bremsstrahlung above n_{crit}, implying additional loss mechanisms play a role.

Spectral broadening mechanisms, such as can result from PDI and wave scattering [18,19], have been suggested as candidate mechanisms for understanding the LH density limit, although there has been no widely accepted unified model to explain the observed loss of LHCD efficiency across multiple

machines [8,9]. Even small upshifts in $n_\parallel$ from these mechanisms can result in significantly lower efficiency since LHCD efficiency is proportional to $1/n_\parallel^2$. On Alcator C-Mod, the onset of PDI has been observed to correlate with the observed loss of efficiency [20]. For example, ion cyclotron PDI are found to be strongly excited above the C-Mod n_{crit} ($\approx 1 \times 10^{20}\ m^{-3}$). It has been previously reported that ion cyclotron PDI can be excited not only near the outer separatrix but also near the inner separatrix of the C-Mod tokamak, depending on the active X-point location [20]. In another diverted tokamak, EAST, ion cyclotron instabilities that exhibit frequencies characteristic of the magnetic field strength near the HFS separatrix have also been observed [21], while the rapid decrease in non-thermal Bremsstrahlung emission is correlated to the PDI onset near the LFS separatrix. Modeling work at FTU reports that ion sound PDI [22] is mainly responsible for the observed density limit in that machine [8,23,24]. In addition to PDI, wave scattering effects have recently been examined with ray-tracing/full-wave approaches [25-28], and could also explain the observed pump broadening on FTU [9,29].

On Alcator C-Mod, the observed loss of efficiency, which correlates well with the ion cyclotron PDI onset, has prevented access to the advanced tokamak operation regime, which requires LHCD operation above n_{crit} to maximize the bootstrap current fraction [30]. At moderate densities ($\bar{n}_e \approx 0.5 \times 10^{20}\ m^{-3}$), fully non-inductive discharges have been demonstrated with current drive efficiency $\eta_{20} \equiv \frac{n_{20} I R}{P} = 0.25\ (10^{20} A \cdot m \cdot W^{-1})$ which is in line with simulations [31], but fast electron populations decrease anomalously above n_{crit}, as indicated by an exponential decrease of hard X-ray count rates. Efficient current drive at these high densities is also crucial to develop a steady-state RF current drive method for reactor-scale experiments, *e.g.*, for ITER, DEMO, or a Fusion Nuclear Science Facility [32], where neutral beams might not be as effective as for existing experimental devices [33]. Therefore, it is important to understand the conditions under which PDI occur and if possible to develop plasma regimes that either avoid their onset or restrict their growth to benign levels.

To better characterize the PDI onset on C-Mod and to further understand its connection to the observed LH density limit, a number of LHCD experiments have been conducted at $\bar{n}_e > n_{crit}$ to examine PDI spectra under various plasma conditions by means of a number of RF probes distributed around the periphery of the C-Mod tokamak. We have mostly given our attention to ion cyclotron PDI activity because it exhibits a density threshold behavior co-incident with the C-Mod n_{crit}. Below this density, the previous modeling based on ray-tracing and full-wave approaches showed that the simulated fast electron production rates are in good agreement with the experimentally measured ones [16]. In this regard, we will not consider scattering effects and/or ion sound PDI because the observed pump broadening on Alcator C-Mod does not exhibit a threshold- like behavior above n_{crit} [35]. Although both could be potentially important together with ion cyclotron PDI in understanding the density limit problem, we do not have any experimental or modeling evidence for this to be the case. Thus, in the remainder of this paper, ion cyclotron PDI will be generally referred to as PDI unless otherwise specified.

Two major results described in this paper will link the onset of PDI with conditions in the plasma edge and Scrape Off Layer (SOL). First, we will show that the previously observed magnetic configuration dependent PDI [20,36] can be generalized to a $\vec{B} \times \nabla B$ configuration dependence, which is explained by the presence of poloidal asymmetries of the SOL density and temperature profiles. Second, we will show that, the PDI onset at the outer wall side best correlates with the observed loss of efficiency, regardless of $\vec{B} \times \nabla B$ configurations, and that it can be controlled by adjusting edge densities, which is achieved by varying plasma current on C-Mod. Increasing the PDI onset density is found to correlate with increased fast electron production at high density. The experimental results presented in this paper build a strong case for a need to minimize parasitic edge-wave interactions for effective LHCD at reactor-relevant densities, which could be achieved by providing low edge densities and enhanced single pass absorption. With this view, discussed at the end of this paper are the implications of off-midplane launch [31,34] and inside launch [37,38], which may be optimal for addressing these issues.

The outline of this paper is as follows. In Section 2, the experimental set up is described with focus on the spectral measurements of lower hybrid waves on Alcator C-Mod. In Section 3, we present the $\vec{B} \times \nabla B$ configuration-dependent PDI onset at $n \sim n_{crit}$, and link it to the change in SOL conditions in diverted plasmas. In Section 4, we show that, regardless of magnetic configurations, the PDI initiated near the outer separatrix are observed well above n_{crit}, and present growth rate analyses to understand the role of edge plasmas on the PDI onset. In Section 5, we describe a plasma current scan experiment and emphasize that the edge plasma density is an important factor in determining the PDI onset. In Section 6, we discuss the implications of these experimental results, and Section 7 presents the conclusions of this paper.

2. Experimental Setup

In Alcator C-Mod, RF spectra in the vicinity of the 4.6 GHz LH applied frequency are monitored by a number of probes installed in the wall of the tokamak, as shown in Figure 1. These probes include several probes mounted in the LH antenna at the outer midplane, and a large number of probes imbedded in lower divertor plates that are toroidally and poloidally separated from the LH launcher. In addition, one of the key probes used in this study was mounted on the inner wall and was originally developed as a scanning probe to monitor parameters in the HFS SOL [39]. It was only used in a fixed position for the RF measurements, and a companion scanning probe was used to monitor density and temperature in the HFS SOL, when available. As shown in Figure 1(b), a small loop antenna was also mounted outside the machine in order to compare PDI results with other LHCD experiments where internal probes were not available [21,23]. Two scanning probes located in the outer wall, labeled ASP and FSP in Figure 1, were used for measurement of plasma parameters (n_e and T_e) in the LFS SOL.

These internal probes were originally designed as Langmuir probes and have slightly different structures. Further, the length of coaxial cables from the probe to the spectral recorder differs among them. Thus, we will not compare the absolute power level of measured frequency spectra among the probes. However, the absolute response of the launcher probe and inner wall probe was measured to be around ~-50 dBm/mW with a dipole antenna when tested on the bench, which was in a reasonable agreement with an analytic calculation. In addition, an in-vessel calibration of the probe at the launcher was conducted with an elbow waveguide that has an aperture at the midsection. By placing the waveguide such that the probe tip is located at the surface of the aperture, we were able to measure the transmission characteristic of the probe, which was in agreement with the dipole antenna measurements and COMSOL simulations. These probes also exhibited a relative flat frequency response in the frequency range of interest without any anomalous frequency resonance behaviors.

To continuously measure LH frequency spectra at multiple locations simultaneously, a purpose-built six-channel, high-repetition rate spectral recorder was used. This system was based on the previously developed spectral recorder [40] used for the LH wave detection by means of reflectometry [41]. It has a sweeping frequency at ~20 Hz, resolution bandwidth of ~ 100 kHz, and frequency bandwidth of ~ 300 MHz near the applied LH frequency at 4.6 GHz. The response of the probe and the spectral recorder was examined in a steady plasma discharge with LH, and the standard deviation of the peak power variation was about 2 dB.

The frequency spectra presented in this paper are measured in diverted plasmas with both forward and reversed toroidal magnetic field direction. In Alcator C-Mod, as shown in Figure 1(b), the standard toroidal field direction is in the clockwise direction when viewed from the top of the tokamak. In the reversed field configuration, the direction of the toroidal magnetic field changes to the counter clockwise direction. The plasma current is always in the same direction as the field, and thus the pitch angle of the magnetic field lines remains the same, regardless of the toroidal magnetic field direction. The purpose of the experiments with the reversed field was to further identify any symmetric behaviors of the PDI onset location by comparing the results obtained in the forward field configuration [20]. Experiments have examined the PDI onset in high density plasmas up to $\bar{n}_e \approx 1.5 \times 10^{20} m^{-3}$ in both lower single null (LSN) and upper single null (USN) configurations. The separatrices of these plasmas are shown in Figure 1(a). In a previous campaign, the density was

typically limited up to $\bar{n}_e \approx 1.2 \times 10^{20} m^{-3}$ with $n_{\parallel}$ =1.6. In more recent experiments the density was increased to $\bar{n}_e \approx 1.5 \times 10^{20} m^{-3}$ and the launched peak $n_{\parallel}$ was increased to 1.9 to avoid the accessibility limit in the density range of interest.

3. Dependence of $\vec{B} \times \nabla B$ Drift Direction at $\bar{n}_e \approx n_{crit}$

In this section, we show that the PDI onset location at $\bar{n}_e \approx n_{crit}$ is dependent on the $\vec{B} \times \nabla B$ drift direction with respect to the active X-point, which can be linked to the presence of poloidal asymmetry in the SOL plasma parameters.

3.1. Spectral Dependence on the Magnetic Equilibrium

Figure 2(a) shows an example of spectra detected by a probe at the inner wall with Alcator C-Mod operating in so-called standard conditions: an LSN equilibrium with $\vec{B} \times \nabla B$ drift direction pointing toward the vertical-wall divertor at the bottom of the tokamak. It shows three frequency spectra at densities spanning n_{crit}. Figure 2(b) shows the corresponding LH frequency spectra normalized to the pump peak amplitudes to better illustrate the relative strengths of the PDI peaks to the pump peaks. The launched peak $n_{\parallel}$ was 1.6 in this case and the plasma current was 550 kA. At low densities, where efficient current drive occurs, very little activity is seen in the spectrum other than the peak at the applied LH frequency, $f_0 = 4.6$ GHz. However, as the density is increased to $\bar{n}_e \approx 0.6 \times 10^{20}\ m^{-3}$, sidebands begin to appear below f_0. As the density is increased to n_{crit}, the sidebands become strong with an energy content comparable to that in the spectrum around f_0 and pump depletion sets in. The spectral peaks, typically 3-4 in number, occur at multiples of the ion cyclotron frequency evaluated near the inner wall ($f_{ci} \sim 60$ MHz). Thus, the sudden decrease in fast electron production and current drive is at least correlated with, if not caused by, the onset of PDI. As the density is increased beyond n_{crit}, for example to $\bar{n}_e \approx 1.3 \times 10^{20}\ m^{-3}$ in the figure, the energy content in the spectrum in the vicinity of the applied frequency drops by about 20 dB while the sidebands become nearly undetectable. In this regime the slow LH wave is marginally accessible inside the separatrix which likely accounts for its 20 dB decrease at the inner wall.

In initially puzzling results, it was found that whenever PDI first appeared, the dominant spectral peaks were always harmonics of a cyclotron frequency, but the cyclotron frequency involved corresponded to the field strength at either the HFS or LFS separatix, depending on the equilibrium configuration. Figure 3 summarizes the radial PDI onset location at $\bar{n}_e \approx n_{crit}$ in four different combinations of the toroidal magnetic field direction and X-point location. The two spectra shown here were measured by the probe at the inner wall, which has been found to be most sensitive to instabilities occurring at the inboard side. By reversing only the direction of the field (and current), and thus $\vec{B} \times \nabla B$, and retaining the same position of the X-point location (LSN), the dominant harmonic frequencies became multiples of the ion cyclotron frequency at the outer (rather than the inner) separatrix. However, by reversing the field *and* current, and changing from LSN to USN, the spectra remained the same as in Figure 2, as expected since the effect of gravity is insignificant and wave propagation behavior should be symmetrical about the mid-plane.

For example, Figure 4 shows LH frequency spectra measured in the USN plasma with the field reversal. The inner-wall probe detects ion cyclotron sideband LH waves that are characteristic of the magnetic field near the inner separatrix at around n_{crit}. This kind of instability is not observed in the LSN plasma (with the field reversal). An interesting feature is that both the probe on the launcher surface and the loop antenna outside the machine are not as sensitive as the inner-wall probe in detecting sidebands excited at the inboard side (e.g., compare spectra at $\bar{n}_e \approx 0.9 \times 10^{20}\ m^{-3}$ and $1.1 \times 10^{20}\ m^{-3}$), implying that those excited sideband LH waves are not likely to propagate toward the LFS edge/outside the machine. Or, it could be simply difficult to distinguish from harmonics of sidebands excited at the LFS SOL because $f_{ci,\ HFS\ SOL} \approx 2\ f_{ci,\ LFS\ SOL}$. Meanwhile, the loop antenna appears to be more sensitive than the launcher probe in detecting sidebands excited at the outer wall (e.g., compare spectra at $\bar{n}_e \approx 1.1 \times 10^{20}\ m^{-3}$). These two observations show that the location of the

probe is important in detecting and interpreting instabilities. Nonetheless, all three probes detect PDI excited at the outer wall well above n_{crit}, and the significance of this will be discussed further in Section 4.

3.2. Poloidal Asymmetry of SOL Densities and Temperatures

The spectral dependence on the magnetic equilibrium turns out to be due to changes in the HFS and LFS SOL conditions that occur when only the direction of $\vec{B}$ (and I_p) is reversed. Because the strong PDI onset at the inboard side is observed only in configurations with the $\vec{B} \times \nabla B$ drift direction toward the X-point, we examined whether the HFS SOL conditions become more favorable for the PDI onset in this configuration. In particular, we examined the poloidal variation of the SOL densities and temperatures because, as will be shown in Section 4.2, the growth rates for PDI are favored by high density and low temperature, and it was indeed found that the conditions in the HFS SOL are more favorable for PDI onset.

Figure 5(a) compares the SOL profiles (pressure, density, and temperature) between the LFS and HFS midplane when the $\vec{B} \times \nabla B$ drift direction is toward the X-point. The profiles are from the Alcator C-Mod Edge Database, and the measurements were done with three of the scanning probes shown in Figure 1: one at the inner wall and two at the LFS side (labeled ASP and FSP). The measurements were taken for Ohmic L-mode plasmas (B_t = 5.4 T, I_p = 800 kA, $\bar{n}_e \approx 1.2 \times 10^{20}\ m^{-3}$). The radial locations are mapped to the outer midplane. In this particular magnetic configuration, a clear poloidal asymmetry of SOL densities and temperatures is observed; as compared with the LFS, the temperature becomes lower at the HFS, and as a result, the densities become higher in order to preserve the pressure (i.e., the product of density and temperature) along field lines. This asymmetry is not observed in the plasma with the $\vec{B} \times \nabla B$ direction away from the X-point; no apparent differences in pressure, density, and temperature profiles are observed between the LFS and HFS, except the general temperature and density variation along the open field lines due to parallel heat conduction.

The cause of this poloidal asymmetry in conjunction with the SOL flow has been extensively studied by Smick [42] and others [43-45]; here we briefly summarize the main conclusion of these studies, which points out the important role of the $\vec{E} \times \vec{B}$ flow. According to these studies, there are two major components that can contribute to the poloidal heat flow, as shown in Figure 5(b). First is the parallel (to the background magnetic field) transport-driven flow, whose source is the turbulent flux transported across the LCFS in the region of unfavorable curvature, i.e., near the LFS midplane. The other is a perpendicular drift-driven $\vec{E} \times \vec{B}$ flow, whose magnitude is generally comparable to or smaller than the parallel heat transport flow. Because the flow direction of the former is X-point dependent and that of the latter is B-field direction dependent, the parallel thermal transport can be reinforced or diminished by the $\vec{E} \times \vec{B}$ flow in the SOL, depending on the direction of $\vec{B}$ and location of the X-point.

Consequently, in the case of LSN or USN equilibria in Alcator C-Mod, with $\vec{B} \times \nabla B$ pointing toward the X-point, the density is higher and the temperature lower in the HFS SOL, and the reverse is true when $\vec{B} \times \nabla B$ points away from the X-point. Smick showed that, with the $\vec{B} \times \nabla B$ pointing toward the X-point, the HFS SOL near the midplane particularly exhibits lower temperatures as compared to the LFS SOL in the density range: $\bar{n}_e \approx 0.8 - 1.1 \times 10^{20}\ m^{-3}$. These observations are in line with previously observed density/temperature asymmetries between the inner and outer divertor target plates with B-field and X-point reversals [43-45] in the density range: $\bar{n}_e \approx 0.5 - 1.5 \times 10^{20}\ m^{-3}$ for Alcator C-Mod plasmas.

This observed linkage of PDI thresholds to conditions in the SOL, as well as the correspondence of the spectral peaks to cyclotron harmonic frequencies near the separatrix, point to the importance of edge conditions in determining PDI onset. In particular, the role of the poloidal density and temperature variation in the SOL needs to be properly considered in diverted plasmas.

The PDI onset at the inboard side is also indicative of weak single-pass Landau absorption of LH waves that are launched at the outer midplane. Modelling of LH wave propagation in Alcator C-Mod high density plasmas shows that the LH waves cross the separatrix several times before a significant $n_{\|}$ up-shift can occur that leads to absorption. This multipass behavior is due to the relatively low core temperature (T_{e0}~ 2 keV). Figure 6 shows an example of ray-trajectories at $\bar{n}_e \approx 1.2 \times 10^{20}\ m^{-3}$ in two different toroidal magnetic field directions with $\vec{B} \times \nabla B$ toward the X-point. The GENRAY/CQL3D ray-tracing/Fokker-Planck code [45,46] is used. In these simulations, a simplified, poloidally symmetric, exponentially decaying SOL model is used, but this will not significantly affect the ray propagation from the launcher to the HFS SOL. It shows that rays launched at the outer midplane propagate toward the inner lower-divertor near the X-point, where poloidal asymmetries are expected to be maximized, rather than toward the inner upper-divertor region closer to the crown of the plasma. Both Landau damping and collisional damping are negligible on the first pass, suggesting that most of the power reaches the HFS SOL, providing a source for instabilities. Thus, this wave propagation together with the SOL conditions are likely to cause the excitation of the PDI at the inboard side. Nonetheless, PDI excited near the inner wall are less threatening regarding current drive since LH waves have to propagate to the inner wall in order for excitation to occur there. This motivates operating LHCD in the "single pass" limit, and this will discussed further in Section 6.

4. PDI Spectra at $\bar{n}_e > n_{crit}$ and Growth Rate Analyses

4.1. PDI Spectra at $\bar{n}_e > n_{crit}$

As the density is increased in C-Mod well above n_{crit}, ion cyclotron harmonics characteristic of the field strength at the outer wall are ultimately observed regardless of the $\vec{B} \times \nabla B$ drift direction with respect to the X-point location. In general, in this density range, neither current drive effects nor evidence of fast electron generation is observed. To examine the strength of the PDI as a function of density, one can define "PDI level" as the relative peak strength of the first down-shifted sideband to the pump peak, as shown in Figure 3.

Figure 7(a) shows both the PDI level excited at the inboard side (in black circles) and the PDI level of excited at the outboard side (in blue squares) as a function of $\bar{n}_e$. Here the plasma has the $\vec{B} \times \nabla B$ drift direction toward the X-point. These spectra are measured with the probe at the inner wall. PDI excited at the HFS SOL dominates over the PDI excited at the LFS SOL in the density range: $\bar{n}_e \approx 0.8 - 1.2 \times 10^{20}\ m^{-3}$, which is in line with the density range where the poloidal SOL asymmetry is observed, as discussed in Section 3.2. However, above $\bar{n}_e \approx 1.2 \times 10^{20}\ m^{-3}$, the energy content of cyclotron harmonics characteristic of the inner wall field strength becomes dominated by PDI frequencies excited near the outer wall (in blue squares and red circles). This can be also clearly seen by examining the frequency spectra at $\bar{n}_e \approx 1.4 \times 10^{20}\ m^{-3}$ in Figure 3; the probe at the inner wall measures harmonics of the ion cyclotron frequency characteristic of the magnetic field at the outer wall. This density corresponds to the density at which the launcher probe begins to detect sideband LH waves initiated at the outer wall side within the detector range, as shown in Figure 7(b). These sideband LH waves detected at the inner wall are expected to have similar $n_{\|}$ to that of the pump, in order to avoid Landau damping on the way from the outer wall side to the inner wall side, as shown in the ray trajectory in Figure 6.

Figure 8 shows the relative peak strength of the sidebands measured with the two probes at the inner wall and at the launcher for the plasma with the $\vec{B} \times \nabla B$ drift direction away the X-point. In this equilibrium, plasma-wave interactions exhibit classical PDI activity; the probes detect ion cyclotron sideband LH waves that exhibit harmonics characteristic of the outer wall field strength, independent of the measurement locations. Interestingly, the probe at the inner wall appears to have a better sensitivity than the probe at the launcher face in detecting these instabilities, although the former is expected to be further away from the PDI excitation location. This could be due to the fact that

sideband LH waves are mostly propagating away from the launcher, and the probe on the launcher surface may not be sensitive enough to detect decay waves at low power levels.

Comparing Figures 7 and 8, one concludes that the strength of the PDI excited at the outer wall best correlates with $\bar{n}_e$, and thus with the loss of current drive efficiency. In particular, Figures 7(a) and 8(a) show that in both configurations, PDI excited at the outer wall are detected with the probe at the inner wall above $\bar{n}_e \approx 0.8 \times 10^{20}\ m^{-3}$. Figure 9 compares the pump peak power and the integrated spectral power of the first-harmonic sideband LH waves. These were measured at three different locations in the LSN equilibria with the field reversal (i.e., $\vec{B} \times \nabla B$ drift direction away the X-point). In this configuration, the observed PDI are initiated at the outer wall side. Instead of integrating the pump within several MHz around the pump frequency 4.6 GHz, we use the pump peak power to represent the power that is expected to have a wavenumber spectrum determined by the launcher. A rapid increase in the sideband power is clearly seen above n_{crit}. With the PDI onset, both the inner wall probe and the loop antenna measure a decrease in pump peak power with density. Well above $\bar{n}_e \approx n_{crit}$, the sideband power saturates and the relative sideband power to the pump is more or less maintained. Here we did not spectrally integrate higher harmonics. The launcher probe measures an increase in the pump peak power by a few dB as the density is increased. The reason for this is not clear, but it may imply that pump power is (back-) scattered due to PDI or additional mechanisms. Even with high single-pass absorption, PDI excited near the outer wall remain a concern since these are expected to occur on the first pass from the launcher to the plasma and then various mechanisms are available for converting the applied power to waves that are ineffective for driving current. In particular, the high frequency PDI daughter waves typically have $n_\parallel \gg n_{\parallel,0}$ and will damp at low temperatures near the edge with negligible current drive efficiency.

4.2. PDI Growth Rate Analyses

In order to understand the conditions under which PDI occur we have examined solutions of the PDI dispersion relation [6,47], which takes the form

$$\epsilon + \frac{(1+\chi_i)\chi_e}{4}\left[\frac{(\mu^-)^2}{\epsilon_1} + \frac{(\mu^+)^2}{\epsilon_2}\right] = 0, \tag{1}$$

where ϵ, χ_i, χ_e are the low frequency dielectric constant and susceptibilities, and $\epsilon_1(\epsilon_2)$ is the dielectric constant for the lower (upper) sideband. The square of the coupling coefficients $\mu^\pm$ depends linearly on the square of the parallel ($\parallel$) and perpendicular ($\perp$) components of the applied (or "pump") electric field ($\vec{E}_0$) as follows:

$$\mu^{\mp 2} = \frac{e}{m_e}\frac{k}{k^\mp}\left(\frac{\left[(\vec{E}_{0\perp}\times\vec{k}_\perp^{\mp})\cdot\hat{z}\right]^2}{\omega_{ce}^2\omega_0^2} + \frac{\left(k_\parallel^\mp\right)^2 E_{0\parallel}^2}{\omega_0^4}\right) \tag{2}$$

where e, m_e is the electron charge and mass, $\vec{k}, \vec{k}^-, , \vec{k}^+$ are the wave-vectors of the ion mode, lower sideband and upper sideband LH waves. The matching conditions dictate the parametric dispersion relation: $\vec{k}^\pm = \vec{k} \pm \vec{k}_0$ and $\omega^\pm = \omega \pm \omega_0$ where $\vec{k}_0$ is the wave-vector of the pump. In C-Mod plasmas, the most unstable solutions to (1) are associated with the excitation of ion cyclotron quasi-modes ($\omega \approx n\omega_{ci}$), whose growth rates are found to be dominant over the ion sound quasi-mode branch ($\omega \approx k_\parallel v_{ti}$). Here, we will not distinguish ion cyclotron quasi-modes from non-resonant quasi-modes ($\omega \approx k_\parallel v_{te}$) that are driven by non-linear electron Landau damping [6]. For C-Mod edge plasmas, both of them tend to coexist in the similar real frequency space, and growth rate calculations show that both can contribute to growth rates with comparable magnitudes ($|\chi_{i,I}| \approx |\chi_{e,I}|$). We also note that in both experiment and calculation strong excitation occurs for $\omega/\omega_{LH} \lesssim 4$, where ω_{LH} is evaluated in the near SOL. Although excitation by $|E_\perp|^2$ is stronger than by $|E_\parallel|^2$, parallel coupling may play a more important role at the plasma edge because the excited

sidebands can propagate nearly parallel to the pump which maximizes their convective amplification. More extensive analysis of PDI growth rates including a discussion of convective effects can be found in [49].

Comparing homogeneous growth rate spectra with the observed frequency spectra indicates that the ion cyclotron quasi-modes are excited at the cold plasma edge with $k_{||}c/\omega_0 \lesssim 10$, where $k_{||}$ is the parallel wavenumber of the ion mode. Figure 10 shows the maximum growth rate and the corresponding real frequency when $k_{||}c/\omega_0$ is varied. All other parameters are kept the same: B_t = 8 T, n_e = 1x10^{20} m^{-3}, $T_e = T_i$ = 25 eV, f_0 = 4. 6 GHz, $n_{||,0}$ =2, $E_\perp$ = = 525 kV/m, and $E_\parallel$ = 0 V/m. The growth rate increases with $k_{||}c/\omega_0$ until the electron Landau damping term becomes significant. The growth rate is maximized near $k_{||}c/\omega_0 \sim 25$, and the corresponding real frequency is about four times the ion cyclotron frequency. The peaking at higher ion cyclotron harmonics is due to the presence of non-resonant quasi-modes, whose real frequency is proportional to $k_\parallel$. Nonetheless, the observed frequency spectra shows the peaking at the first harmonic, and therefore the parallel refractive index of the measured sideband LH waves is expected to be bounded in the range $n_\parallel^- \lesssim 10$. The high-$n_\parallel$ decay waves with a large frequency shift from the pump frequency may not have a significant convective growth because the two resonance cones of the pump and sideband LH waves would be poorly well aligned since the resonance cone angle is a function of the frequency ($e.g.,\ v_{g0\perp}/v_{g0\parallel} \sim \omega_0/\omega_{pe}$). Another possibility is that those high $n_\parallel^-$ sideband LH waves may not have propagated to the probe because of strong Landau damping and they could have been absorbed to the plasma close to where they are excited.

An example of maximum growth rate and real frequency of the ion cyclotron quasi-modes as determined from the local PDI dispersion relation is shown in Figure 11 (c) for an Alcator C-Mod edge plasma. It is assumed that $n_{||,0}$ =2 and $k_{||}c/\omega_0 = 7$. Fits to measured SOL and near-separatrix density (Figure 11 (a)) and temperature (Figure 11 (b)) profiles at the outer wall at $\bar{n}_e \approx 1.2 \times 10^{20}\ m^{-3}$ were used to provide the parameters needed in Equation (1). Growth rates increase with density, due to the enhancement of the perpendicular electric field, and decrease with temperature due to the weakening of the driving term [6]. As a result, the growth rate profile is peaked near the separatrix. From the growth rate calculations one can see that strong growth is limited to the first few ion quasi-mode harmonics near and outside the separatrix. As the separatrix is crossed and the temperature increases, the growth rates become most unstable at higher real frequencies due to the non-resonant quasi-modes ($\omega \propto v_{te}$). But, the magnitude of the growth rates decreases as temperature increases. Only 3-4 harmonics have been observed in the spectral measurements, thus adding support to the conclusion that the most intense PDI are generated in, or very close to, the near SOL. Since the analysis of growth rates from the PDI dispersion relation suggests that reducing the SOL density could mitigate their growth, it led us to conduct the following experiment to examine the change in PDI strength with a different ratio of edge to SOL density.

5. Dependence of PDI Onset on Edge Density

One convenient way to actively control the edge density on C-Mod is to increase the current, since the density in the far SOL of Ohmic L-mode plasmas is found to decrease with decreasing Greenwald fraction [50]. Figure 12 shows the result of a current scan for the three currents at 0.55, 0.80 and 1.1 MA. USN equilibria in the forward magnetic field configuration, i.e., $\vec{B} \times \nabla B$ away from the X-point, were intentionally chosen to focus only on the instabilities occurring at the outer wall. The magnetic field was at 5.4 T and the launched peak $n_\parallel$ was 1.9. A linear density ramp increasing the density from $\bar{n}_e$ = 8x10^{19} m^{-3} to 1.4x10^{20} m^{-3} was programmed and was essentially the same for the three currents. The applied net LH power was kept at around 300 kW for the purpose of outer gap control to enable the scanning probe at the LFS midplane to plunge to the LCFS in order to document SOL temperature and density profiles. The outer gap distance was maintained to be the same in all three discharges, and was linearly decreased from ~1.6 cm at 0.6 second to ~1.2 cm at 1.4 second within a shot. The bottom three spectrograms in Figure 12 are frequency and time- interpolated spectrograms recorded by the

probe at the launcher surface. It can be seen that, with increasing plasma current, the onset of PDI is delayed in time, and therefore at higher line-averaged densities. Both the inner-wall probe and the loop antenna exhibit similar features. In the I_p = 0.55 MA case, ion cyclotron PDI excited at the outer wall are detected after 0.8 second, corresponding to $\bar{n}_e \approx n_{crit}$. In the highest current case (I_p = 1.1 MA), however, ion cyclotron instabilities are detected after 1.2 second, corresponding to $\bar{n}_e \approx 1.3 \times n_{crit}$. Note also that the pump spectrum itself remains sharp in this case as compared to the observed pump broadening in the low current case.

As the current was stepwise increased, scanning probe data revealed a reduction in SOL density as expected. Figure 13 compares the SOL density and temperature measurements for three different discharges at $\bar{n}_e \approx 1.4 \times 10^{20}\ m^{-3}$, which were measured at 1.35 seconds in all three discharges. Due to the presence of the outer limiter at 1.2 cm away from the separatrix, there is a feature that shows a decrease in density around this radial location. The location of the LH launcher was approximately 2 cm from the LCFS as indicated by the dashed lines in Figure 13. The launcher has its own private limiter and its effect is not shown here since the scanning probe measurement's toroidal location is different from the launcher position, as shown in Figure 1. While the density at the separatrix remains essentially the same in all discharges, a clear decrease in SOL densities was observed with increasing plasma current. In the lowest plasma current case (I_p = 0.55 MA), the SOL density profile flattens out toward the far SOL, which is expected to result in higher instability rates and enhanced convective growth. In addition to scanning probe measurements, Langmuir probes mounted in the launcher face also showed a marked decrease in the density at the antenna with increasing plasma current.

No significant changes in temperatures were observed during this current scan, as shown in Figure 13(b). The temperature profiles are rather stiff because the parallel heat conduction coefficient is a strong function of temperature ($\kappa_{||} \sim T_e^{5/2}$), and the changes in the Ohmic power with plasma current were not sufficient to result in a large variation in temperatures. Note that a slightly higher temperature in the lowest current case (I_p = 0.55 MA) is due to the increase in particles in the SOL, which can efficiently convect the heat radially outward. These profile measurements indicate that the observed PDI onset above n_{crit} is indeed a density dependent effect.

Figures 14 (a) and (b) plot the PDI strength as a function of $\bar{n}_e$ and the density measured at the launcher. Here, the PDI strength is defined as the integrated spectral power of the first down-shifted harmonic of the ion cyclotron sideband LH waves. Figure 14 (a) clearly indicates that a global plasma parameter, $\bar{n}_e$, is not determining the PDI onset. As shown in Figure 14 (b), the density at the launcher was approximately the same at PDI onset for the three cases, supporting the inference that a local plasma parameter is the determining factor of the PDI onset. Nonetheless, one needs to be cautious in relating the PDI strength to the density at the launcher as it is not clear where the exact PDI onset location takes place, although it is expected to be between the separatrix and launcher. In this paper, we chose the launcher density as a representative value of the SOL condition because it was the only SOL density variable that could be continuously measured throughout the plasma discharges.

Indications of fast electron production were monitored for these discharges by recording total Bremsstrahlung emission count rate in the energy range 40 – 200 keV and the results are shown in Figure 15. Comparison with the PDI spectra in Figure 12 again suggests a possible causal relation between the onset of PDI near the outer separatrix and the degradation in the hard X-ray flux. In the I_p = 0.55 MA case, there is a brake in slope in the count rates with the PDI onset at n_{crit} and essentially no fast electron production above $\bar{n}_e \approx 1.2 \times 10^{20}\ m^{-3}$. Furthermore, the pump peak power measured with the inner wall probe rapidly decreases with the onset of PDI activities, as shown in Figure 16. This may imply that much of the power could have been lost due to PDI and could not reach the inboard side, although one needs to be careful in reaching this conclusion since it was a localized measurement. Nonetheless, this apparent decrease is in contrast to the I_p = 1.1 MA case, in which the pump peak power at the inboard side maintains its strength more or less even at high densities. In this case, the hard X-ray count rates increases by more than an order of magnitude as compared to the low

current case, which cannot be solely explained by enhanced Landau damping due to a higher temperature. It is expected that other parasitic edge-wave interactions are also minimized due to a reduced SOL density in the multi-pass damping regime.

Improvements in the "density limit" and their correlation with PDI suppression have been reported in LHCD experiments in FTU [11] and EAST [12]. Both machines made use of lithium coating and special fueling methods to reduce wall recycling. However, it should also be also mentioned that Tore Supra has had success in mitigating the falloff in fast electron Bremsstrahlung using pellet fueling, but without a strong correlation with the presence of PDI [51].

6. Implications for future LHCD experiments

In this paper, the onset of PDI has been discussed in conjunction with the LH density limit. The results presented here and from other machines build a strong case for the role played by plasma edge conditions in limiting the density at which LHCD ceases to be effective. In addition to PDI, other undesirable parasitic effects occur in or near the SOL, for example $n_\parallel$ upshift by scattering from edge turbulence and non-specular reflections, and elastic and inelastic collisions. In this section, we discuss two approaches which could be pursued to improve the effectiveness of LHCD in future devices.

The RF power in most LHCD experiments is injected from a mid-plane port. Consequently the rays emanating from the coupler necessarily follow a path on which $n_\parallel$ initially downshifts, making it unlikely that the rays will be absorbed before reaching the HFS SOL. This downshift is a consequence of both toroidal and poloidal effects and is unavoidable when LHCD waves are injected from the midplane. However it has been known for many years that ray trajectories can be optimized by moving the launcher off the midplane [25]. For example, in the case of standard C-Mod equilibria, moving the launch point above the midplane results in an upshift in $n_\parallel$ as the rays propagate radially inwards toward the plasma core, which encourages higher "single-pass" absorption and avoids multiple interactions with the SOL. A new coupler (LH3) has been designed for Alcator C-Mod LHCD experiments to explore the advantage of off-midplane launch [31,34], and useful synergies are expected to occur between the fast electrons produced by LH3 and the present midplane launcher. While difficult to achieve in existing experiments, high single-pass absorption will be the case for reactors owing to their high temperatures, given the Landau damping condition $T_e(0) \gtrsim 40/n_\parallel^2$ where $T_e(0)$ is in keV.

Moving a lower hybrid launcher off the mid-plane to optimize ray trajectories motivates considering the possibility to locate the launcher on the inner wall, especially for tokamaks with double null equilibria [37, 38]. It is not clear in a reactor application of lower hybrid current drive that one can control the density and temperature in the LFS SOL in order to provide a proper impedance match for the coupler and transmission path for the rays. The distance between coupler and separatrix must be many cm's thick in order to provide an effective buffer between the antenna and the reacting plasma. However the LFS SOL is highly turbulent and this presents a possibly insurmountable issue in providing a reliable and predictable ray path with minimal PDI excitation and spectral broadening. While methods exist for transient control of SOL parameters, e.g., lithium deposition and pellet injection, they are not likely to be applicable for the very long pulse or steady state conditions required in a reactor. In fact, locating an LHCD launcher in the LFS SOL where $\omega_p > \omega_0$, i.e., above the cutoff layer, may not be feasible at all for steady-state reactor grade plasmas due to the unpredictable fluxes of energy and particles that would continuously erode the face of the launcher. The HFS SOL in double null configurations would provide far more favorable edge conditions for an LH launcher. For example, as shown in Figure 17 (a), the HFS SOL in Alcator C-Mod exhibits a sharp decrease in density because the particle flows along the field lines from the LFS are disconnected by the presence of the two X-points. As a result, unlike in the single null case (with $\vec{B} \times \nabla B$ drift direction to the X-point) where favorable conditions for PDI occur on the HFS, in double null the PDI growth rates on

the HFS stay well below than those at the LFS SOL, as shown in Figure 17 (b). In this calculation, the same power density is assumed for both the LFS and HFS calculations. A higher magnetic field at the HFS SOL also weakens the ExB driving term, i.e., the first term in the parenthesis in Equation 2. While the temperature is relatively lower at the HFS SOL than at the LFS SOL, the lower density and higher field can overcome the effect of lower temperature, resulting in lower growth rates. Furthermore, a steep density gradient will minimize convective growth due to the thin SOL region and due to the mismatch in the three-wave matching condition [5,22]. Finally, negligible fluctuation levels as compared to those at the LFS SOL will minimize the broadening of the resonance cone and thus the convective growth of sideband LH waves. These favorable edge conditions suggest that the inside launch could be an optimum location to ameliorate PDI effects.

To assess PDI strength at the HFS SOL in double null plasmas, we examined LH frequency spectra in a double null equilibrium, as shown in Figure 18. The launcher was still located at the standard location, i.e., at the outer midplane. As compared to the observed frequency spectra in a single null plasma shown in Figure 4, the probe at the inner wall detects very little PDI activities initiated near the inner separatrix at $\bar{n}_e \approx n_{crit}$, implying that the HFS SOL condition might be favorable to suppress the PDI onset there for the reasons discussed above. Above n_{crit} the frequency spectrum is eventually dominated by PDI at the outer wall side, similar to what was observed in single null plasmas. However, its strength as measured with the inner-wall probe is somewhat weaker than that observed in Figure 4, and this correlates with the previous observation of a higher hard X-ray count rates in double null plasmas than in single null plasmas [15]. Nonetheless, one needs to be careful when predicting PDI effects with inside launch based only on this result because both the plasma condition and wave propagation would not be same as what they would be with inside launch. An experiment with an inside launcher in double null plasmas will be necessary to fully assess PDI and its relation to HFS SOL conditions and fast electron production. A more detailed aspect of the inside launch, including optimized core penetration and absorption is discussed in [37]. A fully integrated inside launcher design is being incorporated into the conceptual design of the Advanced Divertor Experiment (ADX), a new device being proposed by an MIT-led consortium to develop an integrated approach to managing reactor-relevant heat and particle fluxes [38].

7. Summary and Discussion

In this paper, new results are presented on the role of parametric instabilities in limiting the effectiveness of lower hybrid current drive at high density. While direct proof is still lacking, the circumstantial evidence from these and results from other machines suggests that PDI are involved in the universally observed roll off in LHCD efficiency at high density. The PDI onset observed in Alcator C-Mod are linked to the conditions in the SOL. In equilibria with $\vec{B} \times \nabla B$ pointing toward (away from) the active divertor, PDI initiate in the inner (outer) SOL. This has been explained by asymmetries that occur in the SOL due to the effect of an $\vec{E} \times \vec{B}$ flow near the separatrix. PDI occurring in the LFS SOL are regarded as more problematic since PDI near the HFS SOL can be eliminated by strong single pass absorption so that most of the applied power is dissipated before LH rays reach the inner separatrix. This is the basis for a proposed new off-midplane LH launcher on Alcator C-Mod. As density increases, PDI spectra are dominated by instabilities excited at the LFS SOL. Promising results have been obtained in mitigating the effects of LFS SOL PDI and extending the density range over which fast electrons are generated by taking advantage of the lower SOL densities which occur in higher current C-Mod L-mode plasmas.

Eliminating the onset of PDI in the LFS SOL will require control of the SOL density, which may be difficult or impractical in reactor scale devices. In this regard, placing the launcher on the inner wall in double null equilibria would provide optimum edge conditions to suppress PDI and other turbulent scattering mechanisms. The latter advantage is potentially important not only to provide a reliable, turbulence-free path for the LH rays to propagate from launcher to separatrix, but as well to minimize plasma-material interactions with the launcher.

While the observed onset of PDI activity is well correlated with the decrease in current drive efficiency and fast electron productions at high densities, it is not clear what, if any, PDI-related mechanism is responsible, beyond the obvious one of pump depletion. In a recent finding that will be the subject of a future communication it has been determined that at high density the LH RF power is promptly ($\ll \tau_E$) deposited on the outer divertor, but with the same footprint as in the case of core-absorbed power [52]. This suggests that as the density limit is approached the LH power is absorbed near, but possibly just inside the separatrix. The question is then whether this power is mainly associated with the high frequency decay waves or a spectrally broadened pump. In order to address this question an RF probe capable of resolving the wavenumber of the pump and sidebands in the SOL is being fabricated and will be installed for the next Alcator C-Mod run campaign. Also, in growth rate calculations, the $n_{||}$ of the ion mode is a free parameter, and, as shown in Figure 9, the maximum growth rate is found to be in the range above $k_{||}c/\omega_0 \approx 20$ with a peaking at higher harmonics, unlike the experimentally measured frequency spectra. If excited, these sideband LH waves are likely to be damped where they are excited near the separatrix, and they might not propagate all the way out to the fixed probe. The movable probe mentioned above will be also be used to address this conjecture.

Acknowledgements

This research was conducted on Alcator C-Mod, which is a DOE Office of Science User Facility, and is supported in part by: US Department of Energy, DE-FC02-99ER54512.

References

[1] Yamamoto T. 1983 Non-inductive Current Drive in Tokamaks, *Proceedings of the IAEA Technical Committee Meeting* (*Culham, UK, 1983*) pp 224-249

[2] Santini, A. *ibid.* 278

[3] Hooke, W. 1984 Plasma Phys. Control. Fusion 26 133

[4] Porkolab M et al 1977 Phys. Rev. Lett. 38 230

[5] Takase, Y. *et al* Phys. Fluids **28** (1985) 983

[6] Porkolab M 1977 Phys. Fluid 20 2058

[7] Golant V.E. 1980 (1972) Sov. Phys. Tech. Phys. 16 ; Zhur. Tekh. Fiz 41 (1971) 2492

[8] Tuccillo A.A. et al 2012 Proc. 24th Int. Conf. on Fusion Energy (San Diego, 2012)

[9] Bonoli P. T. et al 2014 Phys. Plasmas 21 061508

[10] Bonoli P. T. et al 2008 Phys. Plasmas 15 056117

[11] Wilson J.R. et al 2009 Nucl. Fusion 49 115015

[12] Shiraiwa S. et al 2011 Nucl. Fusion 51 103024

[13] Hutchinson I.H. et al 1994 Phys. Plasmas 1 1511

[14] Wallace G. M. et al 2010 Phys. Plasmas 17 082508

[15] Wallace G.M. et al 2011 Nucl. Fusion 51 083032

[16] Wallace G. M. et al 2012 Phys. Plasmas 19 062505

[17] Meneghini O. 2011 Full-wave modeling of lower hybrid waves on Alcator C-Mod PhD Thesis Massachusetts Institute of Technology

[18] Andrews P. L. and Perkins, F. W. 1983 Phys. Fluids 26 2537

[19] Andrews P. L. and Perkins, F. W. 1983 Phys. Fluids 26 2546

[20] Baek S.G. et al 2013 Plasma Phys. Control. Fusion 55 052001

[21] Ding B. J. et al 2013 Nucl. Fusion 53 113027

[22] Takase Y. et al 1983 Phys. Fluids 26 2992

[23] Cesario R. et al 2010 Nature Commun. 1 55

[24] Napoli F. et al 2013 Plasma Phys. Control. Fusion 55 095004

[25] Bonoli P T et al 1982 Phys. Fluids 25 359

[26] Peysson Y et al 2011 Plasma Phys. Controlled Fusion 53 124028

[27] Bertelli N et al 2013 Plasam Phys. Control. Fusion 55 074003

[28] Madi M et al 2014 Effect of density fluctuations in the scrape-off layer on the lower hybrid power spectrum, 41st EPS Conference on Plasma Physics (Berlin, Germany, 2014), P1.046
[29] Pericoli Ridolfini V et al 2011 Nucl. Fusion 51 113023
[30] Bonoli P T et al 2000 Nucl. Fusion 40 1251
[31] Shiraiwa S. et al 2013 Nucl. Fusion 53 113028
[32] Chan V S et al 2011 Nucl. Fusion 51 083019
[33] Parker R R et al 2014 RF Actuators for Steady-State Tokamak Development, FESAC white paper, https://www.burningplasma.org/resources/ref/fspp/whitepapers/FESAC-SPpaperInitiatives-Parker.pdf
[34] Wallace G M et al 2013 Nucl. Fusion 53 073012
[35] Baek S G et al 2012 Plasma and Fusion Research 7 2402031
[36] Baek S. G. et al 2014 Phys. Plasmas 21 061511
[37] Bonoli P. T. 2014 To be submitted to Physics of Plasmas
[38] B. Labombard, et. al., FESAC white paper, https://www.burningplasma.org/resources/ref/fspp/whitepapers/FESAC-SPpaperInitiatives-LaBombard.pdf
[39] Smick N and LaBombard B 2009 Rev. Sci. Instr. 80 023502
[40] Baek S.G. et al 2012 Rev. Sci. Instrum. 83 10E325
[41] Baek S. G. et al 2014 Phys. Plasmas 21 012506
[42] Smick N et al 2013 Nucl. Fusion 53 023001
[43] Labombard B. et al 2004 Nucl. Fusion 44 1047
[44] Labombard B. et al 1997 J. Nucl. Mater 149 241
[45] Hutchinson I. et al 1995 Plasma Phys. Control. Fusion 37 1389
[46] Smirnov A.P. and Harvey R. 1995 Bull. Am. Phys. Soc. 40 1837
[47] Harvey R.W. and McCoy M. 1992 Proc. IAEA TCM on Simulation and Modeling of Thrmonuclear Plasmas (Montreal, Canada, 1992) pp 489–526 www.compxco.com/cq13d.html
[48] Liu, C S *et al* 1984 Phys. of Fluids 27 1709
[49] Baek S.-G. 2014 PhD thesis, Massachusetts Institute of Technology
[50] LaBombard B et al 2008 Phys. Plasmas 15 05606
[51] Goniche, M. et al Nucl. Fusion **53** (2013) 033010
[52] Faust, I. et al Bulletin of the American Physical Society **59** PO3.11 http://meetings.aps.org/link/BAPS.2014.DPP.PO3.11

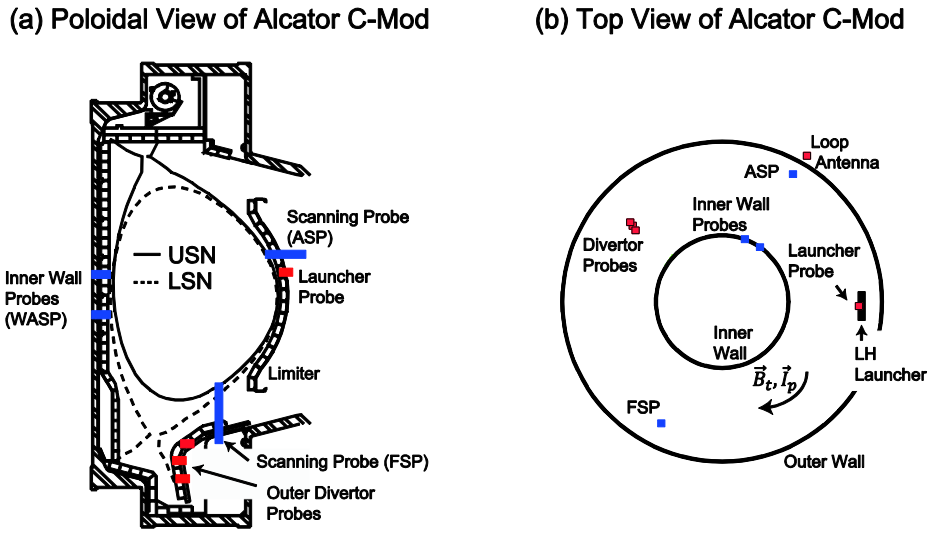

Figure 1: (a) Poloidal and (b) top views of the Alcator C-Mod tokamak, which show the poloidal and toroidal location of both fixed (in red) and scanning (in blue) probes that were used to study lower hybrid waves. The separatrices of both an upper-single-null (USN) plasma and a lower-single-null

(LSN) plasma are shown in (a). The standard direction of the toroidal magnetic (B_t) direction is in the clockwise direction when viewed the tokamak from the top, as shown in (b). The direction of the plasma current (I_p) is always in the same direction as the B_t direction.

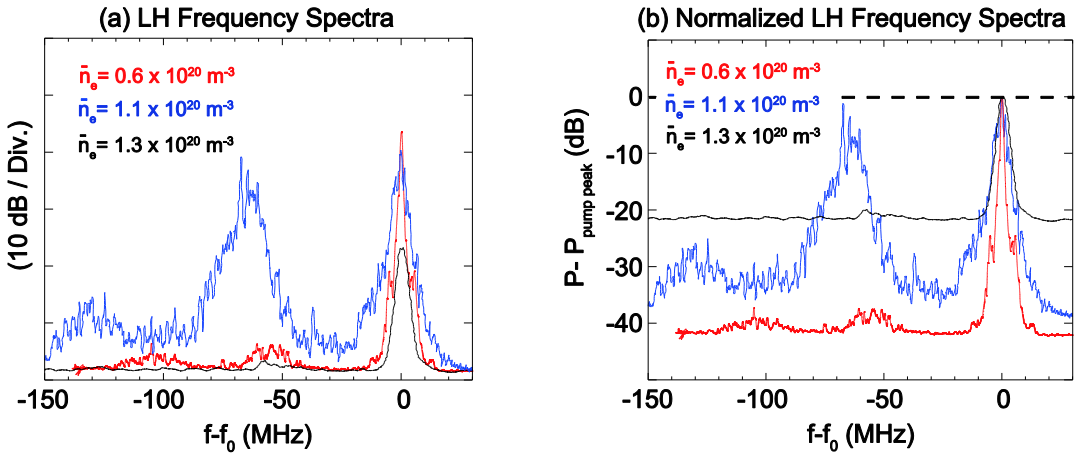

Figure 2: (a) LH wave frequency spectra measured at $\bar{n}_e$= 0.6 x 10^{20} m^{-3} (red), 1.1x10^{20} m^{-3} (blue) and 1.3x10^{20} m^{-3} (black) with the inner wall probe in LSN plasmas in the forward-field configuration (B_{t0} = 5.4 T, I_p =550 kA). The launched wave spectrum is centered at $n_{\|}$ =1.6. Sideband peaks in the spectra correspond to f_{ci} at the high field side edge. Here, f_0 is the applied LH source frequency (4.6 GHz). (b) The corresponding LH frequency spectra normalized to the pump peak amplitudes.

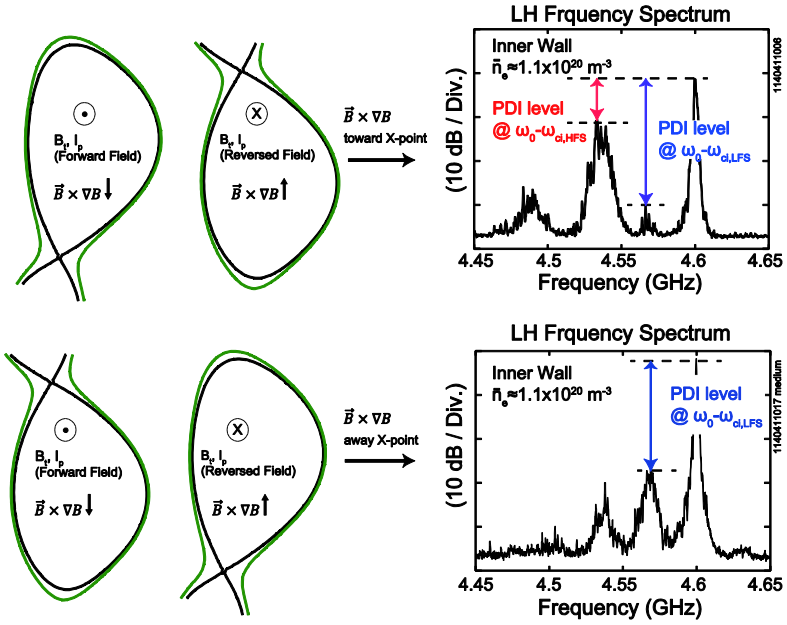

Figure 3: Dependence of the PDI onset location on the $\vec{B} \times \nabla B$ drift direction at $\bar{n}_e \approx n_{cirt}$. B_{t0} = 5.4 T and I_p =550 kA. The spectra are measured with the inner wall probe at $\bar{n}_e$= 1.1 x 10^{20} m^{-3}. In the plasmas with the $\vec{B} \times \nabla B$ drift direction toward the X-point, the spectrum shows instabilities excited at two different radial locations: (1) the first- and second- harmonics of the ion cyclotron PDI excited near the inner wall (f_{ci} ~ 60 MHz) and (2) the first harmonic of the ion cyclotron PDI excited near the outer wall (f_{ci} ~ 30 MHz). On the other hand, in the plasmas with the $\vec{B} \times \nabla B$ drift direction away from

the X-point, the spectrum shows only the harmonics of the ion cyclotron PDI excited near the outer wall (f_{ci} ~ 30 MHz). Here, the PDI level is defined as the relative peak power of the first harmonic of the sideband to that of the pump. The PDI levels are shown as a function in the line-averaged density in Figures 7 and 8.

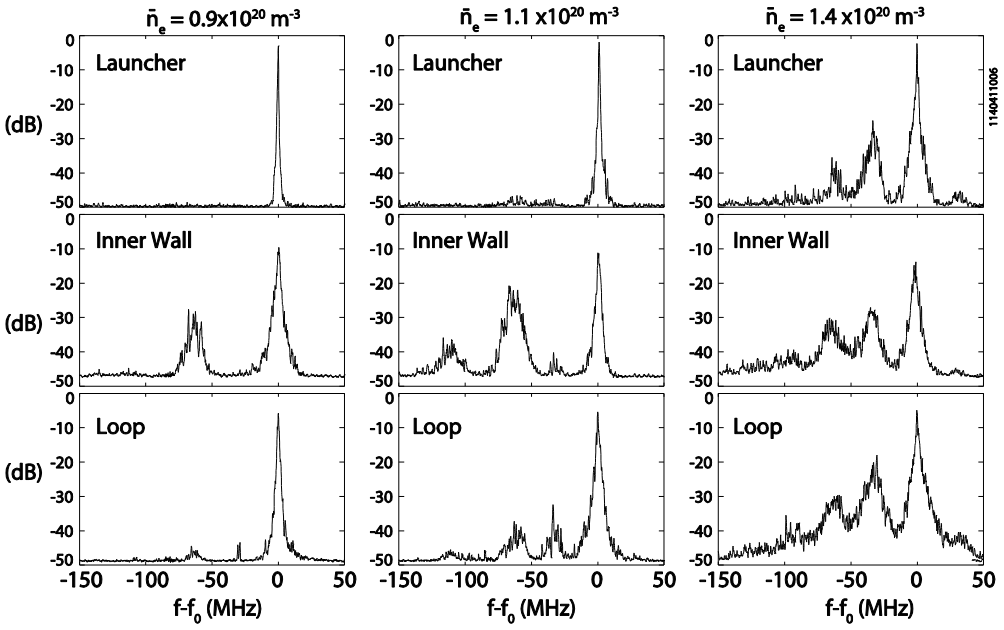

Figure 4: LH frequency spectra at $\bar{n}_e$ = 0.9 x 10^{20} m^{-3}, 1.1x10^{20} m^{-3}, and 1.4x10^{20} m^{-3} measured with the launcher probe, inner wall probe and the loop antenna in the USN plasma with the toroidal magnetic field in the reversed direction (B_{t0} = 5.4 T, I_p =550 kA). Here, f_0 is the applied LH source frequency (4.6 GHz).

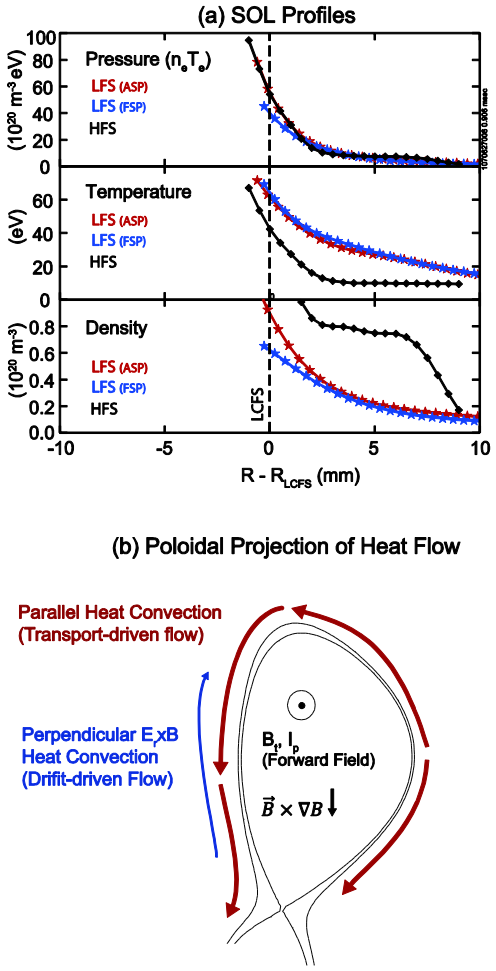

Figure 5: (a) Comparison of the SOL pressure, temperature, and density between the LFS (red and blue) and HFS (black) midplane in a L-mode plasma with $\vec{B} \times \nabla B$ pointing toward the X-point (B_t = 5.4 T, I_p = 800 kA and $\bar{n}_e \approx 1.2 \times 10^{20}\ m^{-3}$). The measurements were done with scanning probes at the LFS (i.e., ASP and FSP, as shown in Figure 1), and at the HFS (i.e., WASP). Note that no LH was injected in this plasma. (b) A pictorial representation of two dominant polodial flow components: one from the parallel transport-drive flow and the other from the perpendicular $\vec{E} \times \vec{B}$ flow.

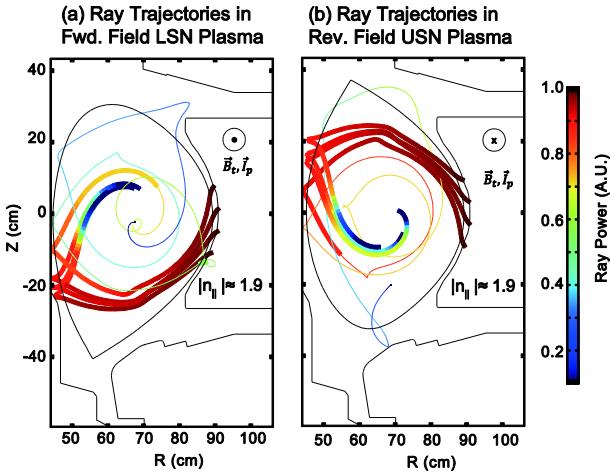

Figure 6: Examples of ray trajectories at $\bar{n}_e \approx 1.2 \times 10^{20}\ m^{-3}$ in two plasmas with $\vec{B} \times \nabla B$ toward the X-point: (a) LSN plasma with the forward field configuration and (b) USN plasma with the reversed field configuration. The rays are launched with $n_{||} = 1.9$ at four different poloidal locations to simulate the four rows of the Alcator C-Mod launcher geometry. In both cases, $B_{t0} = 5.4$ T, and $I_p = 550$ kA. Each ray power is normalized to the initial ray power. For the visualization purpose, the rays that undergo multiple bounces are marked with thinner lines after the reflection at the inner wall.

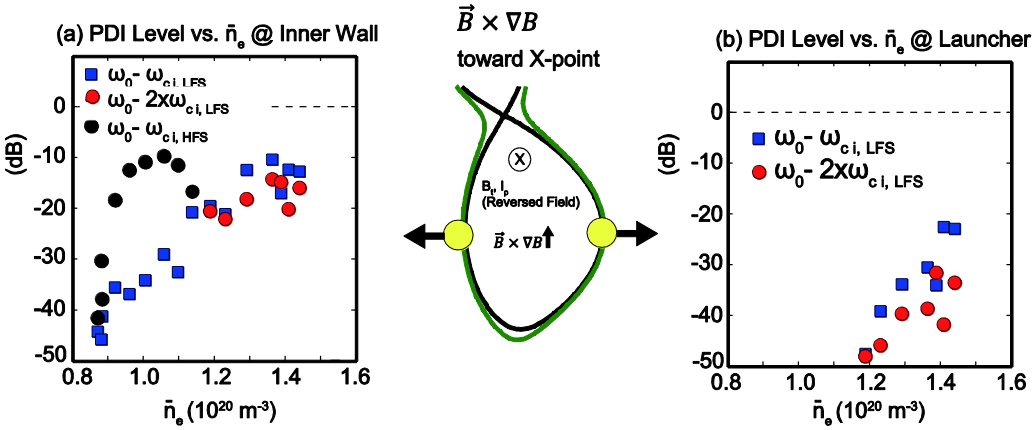

Figure 7: (a) Inner wall probe measurements of the relative peak powers of the sidebands that are characteristic of the magnetic field at the inner wall (in black circles) and at the outer wall (in blue squares) in the plasma with the $\vec{B} \times \nabla B$ pointing toward the X-point. Note that $f_{ci,\ HFS\ SOL} \approx 2xf_{ci,\ LFS\ SOL}$. The red circles above $\bar{n}_e \approx 1.2 \times 10^{20}\ m^{-3}$ denote the second harmonic of the instabilities excited at the outer wall (e.g., refer to the frequency spectrum measured with the inner wall probe in Figure 3). (b) Launcher probe measurements of the relative peak powers of the sidebands that are characteristic of the magnetic field strength at the outer wall (in blue squares) and the second harmonics (in red circles).

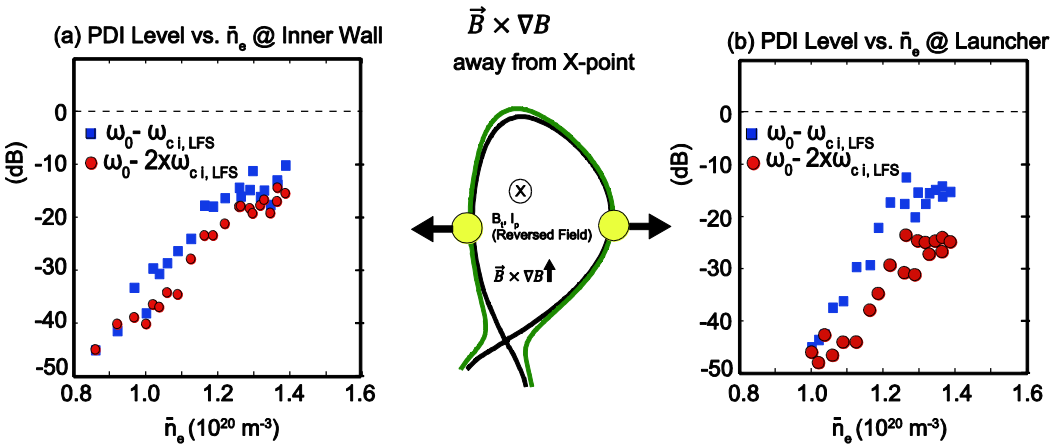

Figure 8: (a) Inner wall probe measurements of the relative peak powers of the sidebands that are characteristic of the magnetic field strength at the outer wall (in blue squares) and the second harmonics (in red circles) in the plasma with the $\vec{B} \times \nabla B$ pointing away from the X-point. (b) Launcher probe measurements of the relative peak powers of the sidebands that are characteristic of the magnetic field at the outer wall (in blue squares) and the second harmonics (in red circles). As

compared to Figure 7, the inner wall probe does not detect PDI with peaks characteristic of the magnetic field strength at the HFS.

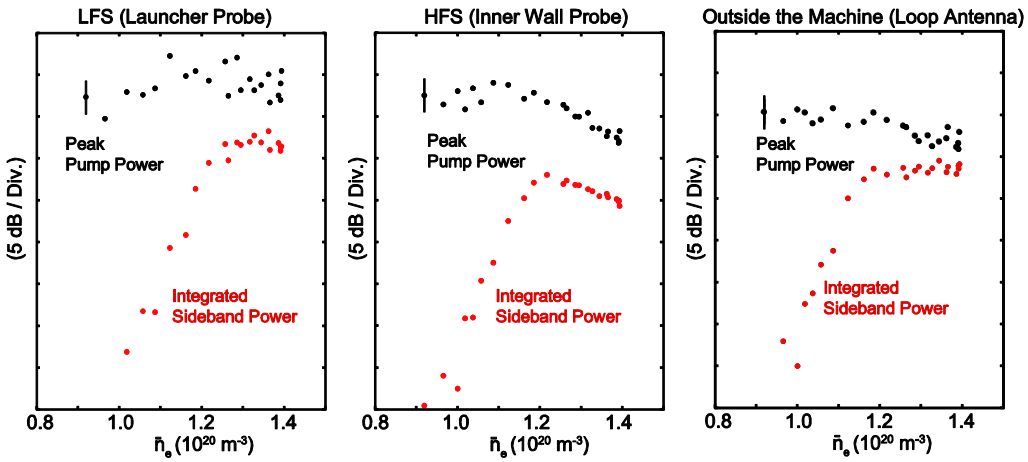

Figure 9: Pump peak power and the integrated sideband power of the first-harmonic sideband LH waves measured at (a) the launcher, (b) the inner wall, and (c) outside of the machine. LSN equilibrium with the field reversal (i.e., $\vec{B} \times \nabla B$ drift direction away the X-point). I_p = 550 kA.

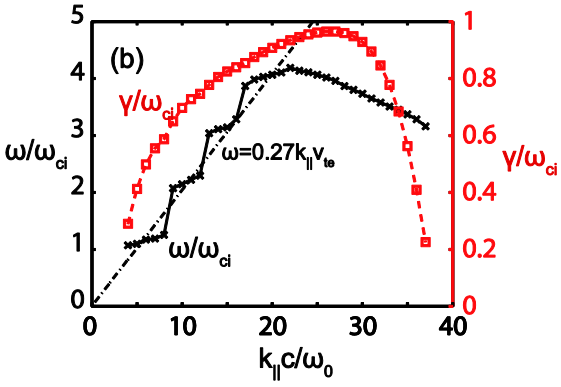

Figure 10: Dependence of the maximum growth rate and the corresponding real frequency as a function of the normalized parallel refractive index of the ion mode ($k_{||}c/\omega_0$). B = 8 T, $n_e = n_i = 10^{20}$ m^{-3}, $T_e = T_i$ = 25 eV, f_0 = 4.6 GHz, $ck_{0||}/\omega_0 = 2$, $E_\perp$ = 525 kV/m, and $E_{||}$ = 0 kV/m. The straight line corresponds to $\omega_{R,max} \approx 0.27k_{||}v_{te}$, and its slope shows the quasi-mode nature of the ion mode.

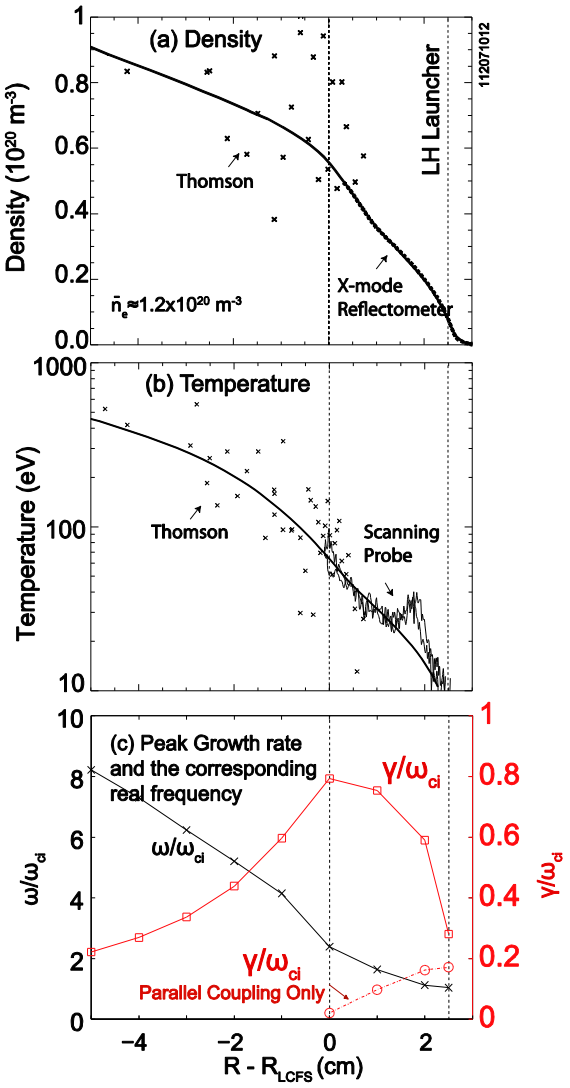

Figure 11: (a) Measured edge density profile with a Thomson scattering diagnostic and X-mode reflectometer in front of the launcher in a USN L-mode plasma at $\bar{n}_e \approx 1.2 \times 10^{20}\ m^{-3}$ with forward field configuration. The line shows the fitted edge density profile. (b) Measured edge temperature profile. The line shows the fitted edge temperature profile. The bump in the SOL temperature profile is thought to be real, but the reason for it is not clear. (c) Dependence of the maximum growth rate (red) and the corresponding real frequency (black) of the ion cyclotron quasi-modes on the radial locations. The red solid curve is the maximum growth rate when both the perpendicular and parallel coupling terms are retained. The red dashed curve is the maximum growth rate when only the parallel coupling term is retained. f_0 = 4.6 GHz, $ck_{0\|}/\omega_0 = 2$, $ck_\|/\omega_0 = 7$, and P_{RF} = 100 kW for a single row of the launcher.

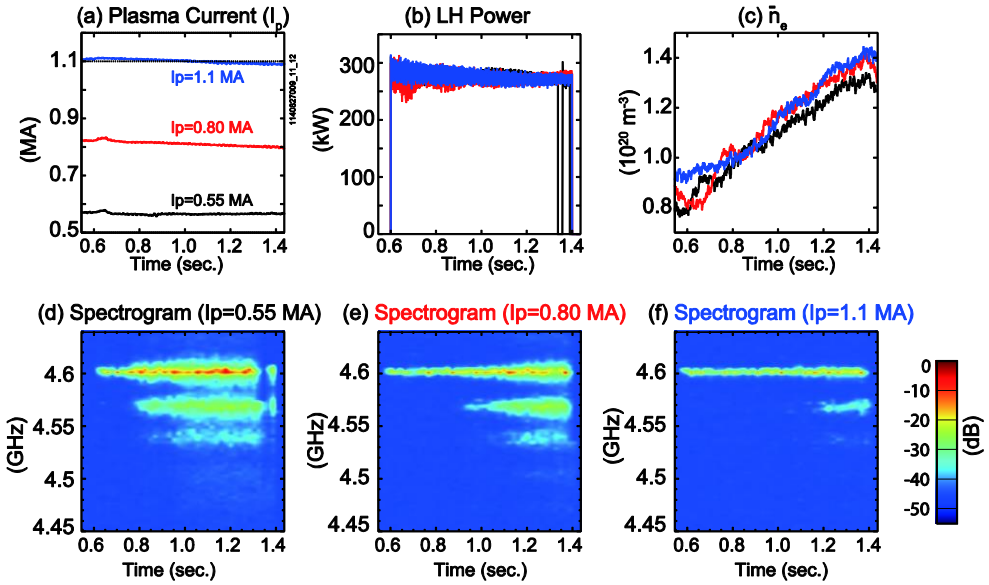

Figure 12: Top row: Time traces of (a) plasma current, (b) LH power, and (c) line-averaged density for plasma discharges at three different plasma currents: 0.55 MA (black), 0.8 MA (red) and 1.1 MA (blue). Bottom row: time- and frequency- interpolated spectrograms measured with the launcher probe at (d) 0.55 MA, (e) 0.8 MA, and (f) 1.1 MA.

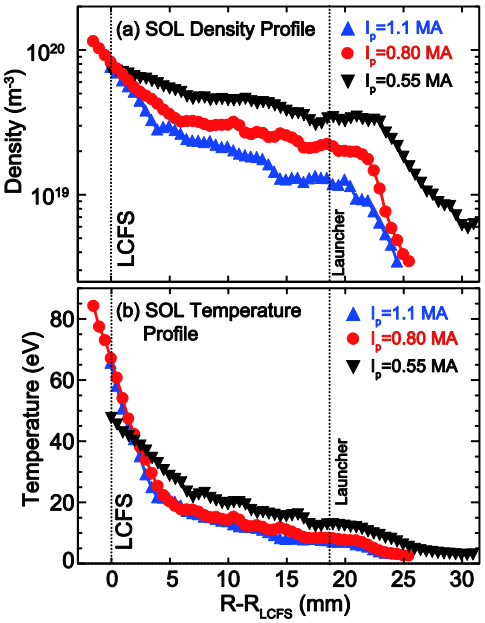

Figure 13: SOL (a) density and (b) temperature profiles at $\bar{n}_e \approx 1.4 \times 10^{20}\ m^{-3}$ in the three plasmas shown in Figure 12.

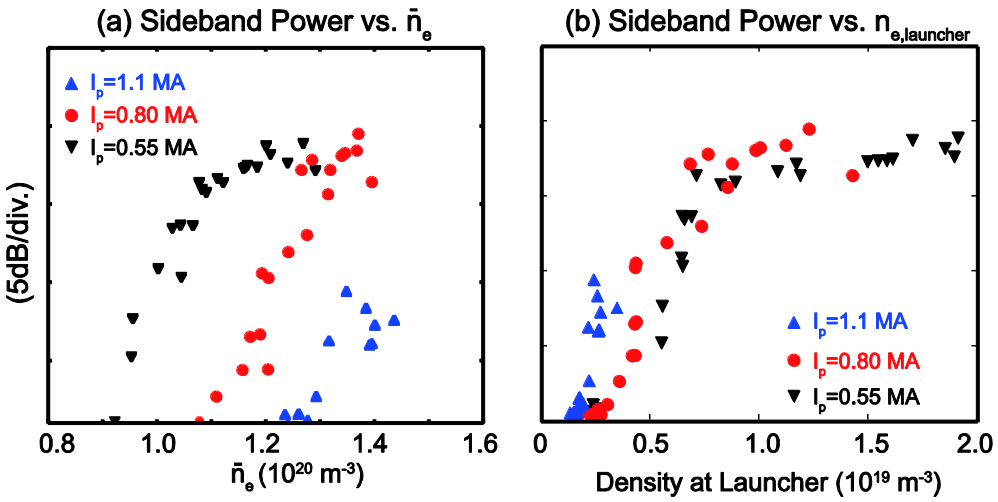

Figure 14: Sideband power versus (a) the line-averaged density and (b) the density at the launcher. Here, the sideband power is the integrated spectral power of the first down-shifted harmonic of the sidebands. They are measured with the launcher probe in the three plasmas shown in Figure 12.

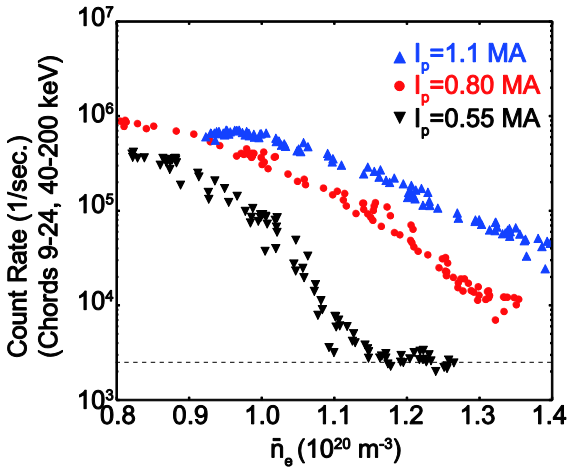

Figure 15: Non-thermal bremsstrahlung emission rate as a function of the line averaged density in the plasmas at three different plasma currents at 0.55 MA (black), 0.8 MA (red), and 1.1 MA (blue) as shown in Figure 12. The horizontal dashed line shows the noise floor of the hard X-ray diagnostic.

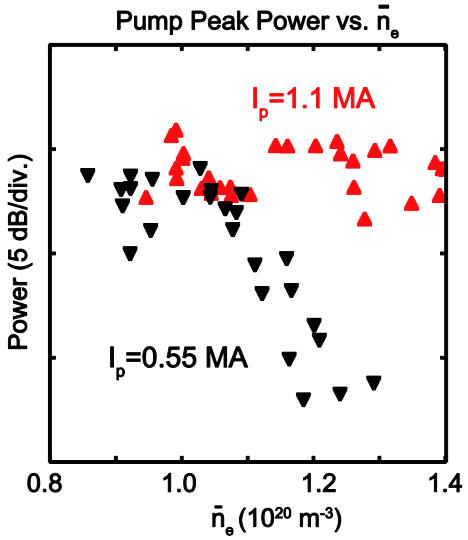

Figure 16: Pump peak power at the inboard side measured with the inner wall probe in the plasmas shown in Figure 12.

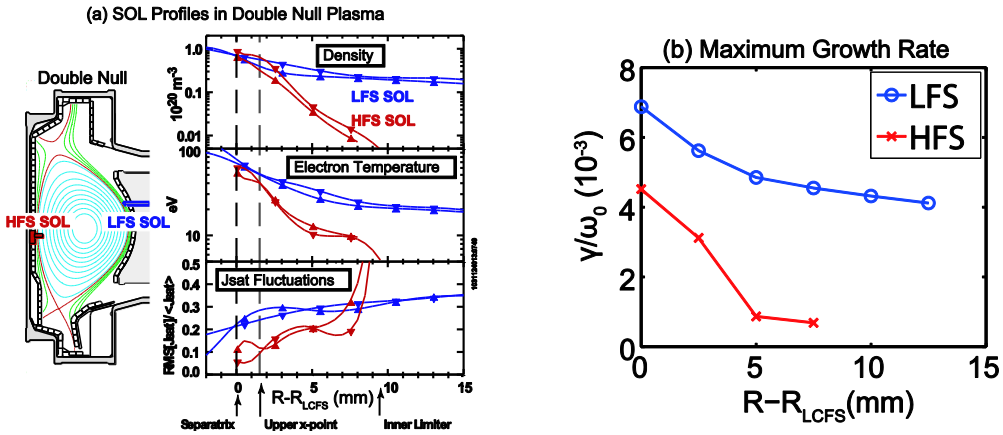

Figure 17 (a): SOL profile comparisons between the LFS (blue) and HFS (red) midplane in a double null plasma. Ohmic L-mode plasma, B_t = 5.4 T (forward field configuration), I_p = 0.78 MA, and $\bar{n}_e \approx 1.4 \times 10^{20}\ m^{-3}$. Figure is reproduced from [43] The double traces correspond to the in and out sweep of the scanning probes. (b) Comparison of the maximum growth rate based on growth analyes using Equation (1) between the LFS (blue) and HFS (red). f_0 = 4.6 GHz, $ck_{0\|}/\omega_0$ = 2, $ck_{\|}/\omega_0$ = 7, Bt = 4 T (8 T) for the LFS (HFS) calculation, and P_{RF} = 100 kW for a single row of the C-Mod launcher. The same power density is assumed for both the LFS and HFS calculations.

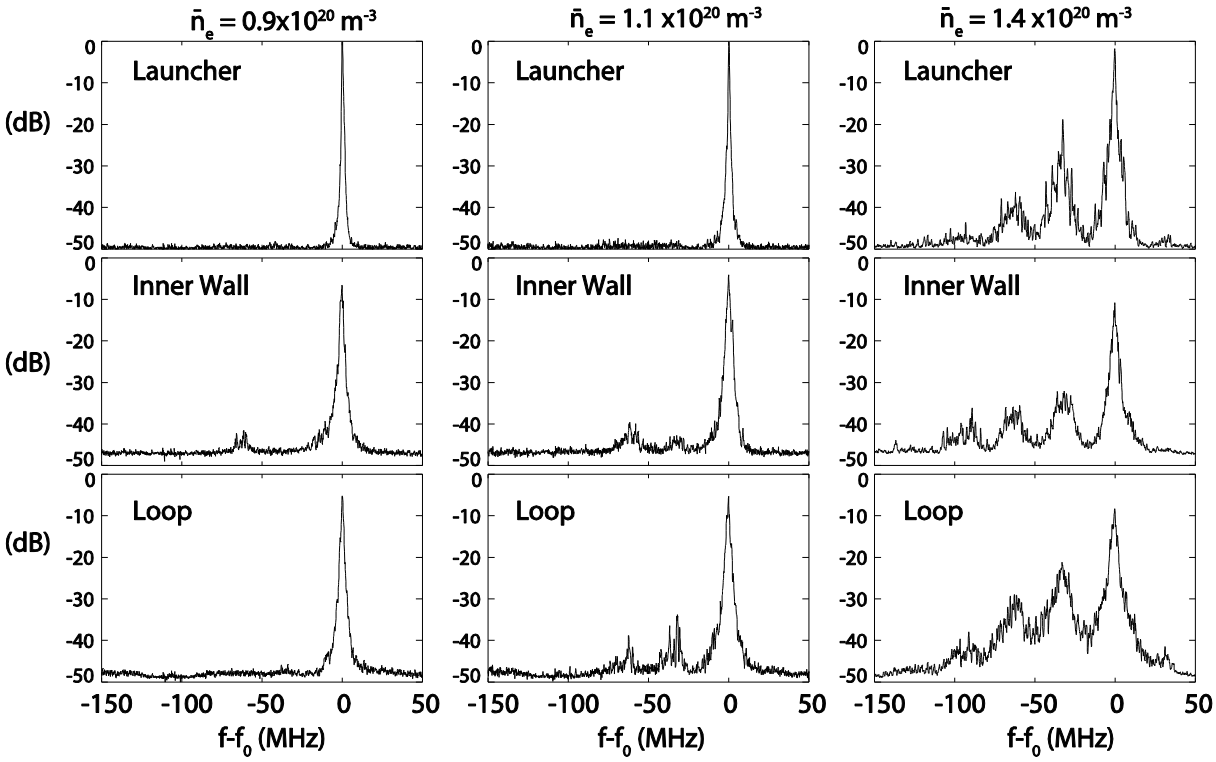

Figure 18: LH frequency spectra at $\bar{n}_e$= 0.9 x 10^{20} m^{-3}, 1.1x10^{20} m^{-3}, and 1.4x10^{20} m^{-3} measured with the launcher probe, inner wall probe and the loop antenna in the double null plasma with the toroidal magnetic field in the reversed direction (B_{t0} = 5.4 T, I_p =550 kA). Here, f_0 is the applied LH source frequency (4.6 GHz)